Chemistry–A European Journal
Research Article
doi.org/10.1002/chem.202300825
Chemistry Europe
European Chemical Societies Publishing
www.chemeurj.org

De-Novo Design of pre-miR-21 Maturation Inhibitors: Synthesis and Activity Assessment

Iryna Shcheholeva,[a] Daniel Fernández-Remacha,[b] Roger Estrada-Tejedor,[b] Maria Duca,*[a] and Véronique Michelet*[a]

Abstract: Targeting RNA with small molecules is a major challenge of current medicinal chemistry, and the identification and design of original scaffolds able to selectively interact with an RNA target remains difficult. Various approaches have been developed based on classical medicinal chemistry strategies (fragment-based drug design, dynamic combinatorial chemistry, HTS or DNA-encoded libraries) as well as on advanced structural biology and biochemistry methodologies (such as X-ray, cryo-EM, NMR, or SHAPE). Here, we report the de novo design, synthesis, and biological evaluation of RNA ligands by using a straightforward and sustainable chemistry combined with molecular docking and biochemical and biophysical studies that allowed us to identify a novel pharmacophore for RNA binding. Specifically, we focused on targeting the biogenesis of microRNA-21, the well-known oncogene. This led us not only to promising inhibitors but also to a better understanding of the interactions between the small-molecule compounds and the RNA target paving the way for the rational design of efficient inhibitors with potential anticancer activity.

Introduction

Pharmacological intervention at the RNA level greatly expands the area of accessible biological targets, and the discovery of specific ligands of therapeutically relevant RNAs is an emerging area of medicinal chemistry that has already shown its potential.[1] Indeed, a large number of antibiotics, such as aminoglycosides or oxazolidinones, are currently on the market as binders of prokaryotic ribosomal RNA, thus inducing the inhibition of protein synthesis in bacteria.[2] More recently, the FDA approval of Risdiplam as a pre-mRNA splicing modifier for the treatment of spinal muscular atrophy (SMA) highlighted that the field of RNA targeting is just at the beginning of what will probably lead to the discovery of innovative therapies for still incurable diseases.[3] Although RNA targeting has gained a great interest in the medicinal chemistry community over the last decades, the search for compounds able to bind to biologically relevant RNAs and selectively alter their function remains challenging.[4] The most straightforward approach to tackle the problem (i.e., antisense oligonucleotides) proved to be an effective solution, as attested by several approved drugs of this class.[5] However, despite numerous signs of progress made in the field, these modalities still have pharmacodynamic and pharmacokinetic liabilities, mostly caused by nucleases degradation and poor biodistribution. In contrast, small molecules often lack these problems, yet their selective mutual recognition with nucleic acids is far less intuitive. Oftentimes, ligands found to target secondary RNA structures do not meet the drug-likeness requirements, and once the lead is identified, its potency is difficult to improve.[6]

Among biologically relevant RNAs, microRNAs (miRNAs or miRs) are short noncoding RNAs acting as gene expression regulators upon recognition of mRNAs and inhibition of protein synthesis. Thousands of miRNAs have already been identified in humans, and each of which is responsible for the regulation of the expression of hundreds of proteins, thus having a pivotal role in cellular homeostasis. However, abnormal levels of some miRNAs have been linked to the development of numerous diseases, such as cancers, and several miRNAs have been identified as oncogenic as their overexpression has been directly linked to cancer development and progression.[7] More specifically, miR-21 and its precursor pre-miR-21 (Figure 1a) have been in the spotlight after its consistent overexpression has recently been reported in a study profiling 540 clinical samples from cancer patients.[8] The inhibition of miR-21 function thus holds the promise for both efficient therapy alone,[9a–f] and as an adjuvant to the existing treatments.[10a–e] The search for small molecule inhibitors of miR-21 is mainly based on the targeting of one of its precursors (pri- or pre-miRNA) that bear secondary structures formed by the presence of single-stranded regions (loop and bulges) that together with double-stranded ones induce the formation of specific RNA binding pockets (Figure 1a). During miRNAs biogenesis, Drosha

[a] I. Shcheholeva, Dr. M. Duca, Prof. V. Michelet
Université Côte d'Azur
Institut de Chimie de Nice (ICN), CNRS
Parc Valrose 06100 Nice (France)
E-mail: maria.duca@univ-cotedazur.fr
veronique.michelet@univ-cotedazur.fr
[b] D. Fernández-Remacha, Dr. R. Estrada-Tejedor
IQS School of Engineering, Universitat Ramon Llull
Via Augusta 390, 08017 Barcelona (Spain)

Supporting information for this article is available on the WWW under https://doi.org/10.1002/chem.202300825

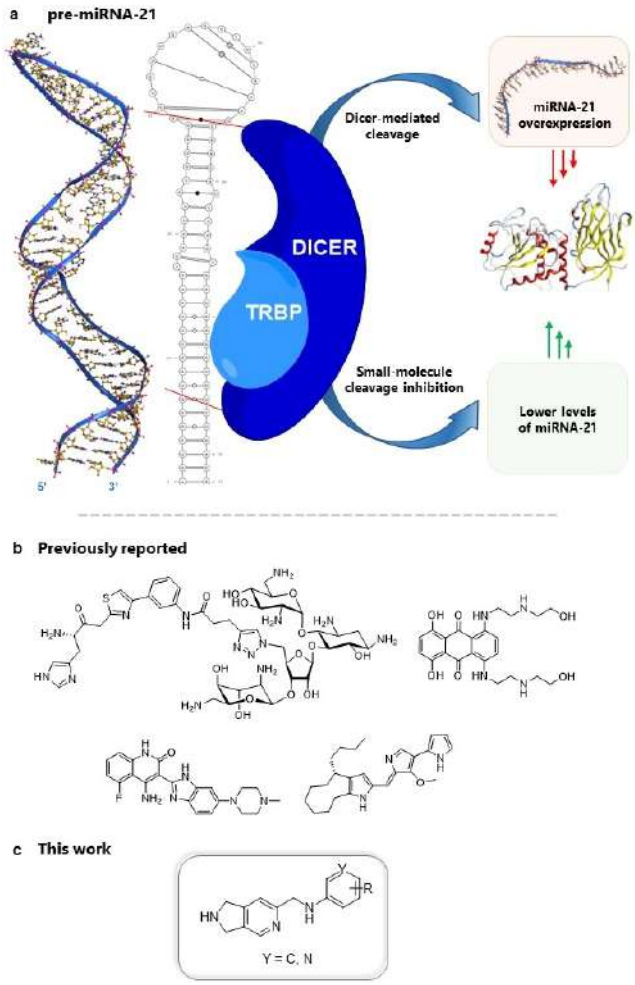

Figure 1. Inhibition of miR-21 biogenesis by using synthetic small molecules. a) 3D model and schematized structures of pre-miR-21 containing double- and single-stranded regions (a single line corresponds to an AU pair, a double line to a GC pair, and a single line with a dot to mismatches). If a Dicer protein complex cleaves the pre-miRNA-21, mature miRNA-21 is produced, decreasing the translation of tumor-suppressor proteins (the example protein is PTEN PDB ID: 1D5R). However if a small molecule inhibits this cleavage, no miRNA will be produced, restoring the tumor-suppressor protein levels. b) Structures of compounds reported in the literature to inhibit miR-21 biogenesis upon binding to pri- or pre-miR-21. c) The new scaffold presented in this work.

and Dicer ribonuclease cleave the precursors, called pri-miRNAs and pre-miRNAs, respectively, leading to mature miRNAs, but small molecules can bind to the precursors and selectively inhibit miRNA biogenesis. This concept has already been successfully applied in the literature and, in particular, against miR-21 biogenesis.[11a–e] Most of the ligands reported so far to inhibit miR-21, indeed, act by impeding the processing of pre-miR-21 by Dicer (Figure 1b).

During recent years, we developed a multimodal approach for the design of RNA ligands and, in particular, for the discovery of oncogenic miRNAs inhibitors.[11e–d,12a–b] Merging different RNA binding domains in one molecule brought both affinity and selectivity for the target and led us to the identification of compounds capable of inhibiting the biogenesis of oncogenic miRNAs in vitro and showing antiproliferative activity in cancer cells with overexpressed targeted miRNA. Although the compounds were not specific for one miRNAs, they were able to selectively target a small set of oncogenic miRNAs and led to a very specific biological effect. Therefore, this multimodal approach thus led to promising results, but the synthetic pathways needed to prepare the compounds were long and tedious, while the compounds themselves bear high molecular weight and unfavorable physicochemical properties for future applications.[11d,12b]

Here, we report the de-novo design of new RNA binders, focusing our effort on developing miR-21 inhibitors bearing good affinity and selectivity but also drug-like properties and synthetic accessibility. To this aim, we have chosen to explore dihydropyrrolopyridine as a privileged and unexplored scaffold to prepare new ligands (Figure 1c). A large series of derivatives were designed and then prepared employing an atom- and step-economical synthetic methodology relying on ruthenium-catalyzed [2+2+2] cycloaddition, thus giving access to the desired scaffold for further functionalization.[13–14] We brought to light the activities of novel compounds with micromolar affinity for pre-miR-21 and the ability to inhibit miR-21 biogenesis. The detailed study of the potential mechanism of binding using enzymatic footprinting, molecular modeling, and docking as well as STD NMR allowed us to draw the structure-activity relationships for a completely new class of RNA ligands.

Results and Discussion

Design and synthesis of a new library of RNA binders

The design of a new RNA-focused library of ligands was driven by modularity and reflection on the data reported so far on the miR-21 inhibitors and binders in general.[11a–b,d,15] Decades after the pioneering report on targeting pre-miRNAs with small molecules,[16] the data gathered on the active compounds isn't ample, although some notions of general knowledge in the field are being instilled. Loops and bulges are the primary targets in a search for potential binding sites, being more solvent-accessible and providing more opportunities for the interaction to occur. The logic is supported by the evidence, that the same structures mediate the RNase recognition of the substrate for subsequent processing, thus abrogating their access by direct ligand binding may result in cleavage inhibition. Some compounds have been reported over the last decade as inhibitors of Dicer processing of the pre-miR-21 by direct binding to the pre-miRNA, though, some of them still lack selectivity (Figure 1b).[11a–c,e] De-novo drug design in academic context without several thousand screening libraries at our disposal calls for a careful choice of the starting point. For a purely synthetic approach, referencing known privileged molecular structures can lead to active compounds with a pledge for metabolic stability. Leaning on the broader definition of the privileged scaffold and taking into account the reported RNA binders,[17a–b] we anticipated that the 2-amino-dihydropyrrolopyridine could be a valuable scaffold to construct a new

library, able to interact with the target using the two most favorable interactions found in RNA binders, that is, hydrogen bonds and π-stacking interactions.[17,18] In our continuous research programs towards the preparation of bioactive molecules,[19a–c] and our deep experience in sustainable chemistry, we selected the bicyclic scaffold of dihydropyrrolo-pyridine, which to the best of our knowledge, has never been envisaged as an RNA binder.

The existing synthetic routes to access the scaffold were not ideal for quick library construction, often involving the preparation of individual nitriles. We thus designed two synthetic strategies to allow a straightforward and modular synthesis of a large library of compounds involving only three steps for the preparation of a common building block (**1a** and **1b** in Scheme 1) followed by functionalization and deprotection steps to obtain the desired compounds (**3a–f** and **4a–4x** in Scheme 1). The key step of our strategies is a ruthenium-catalyzed [2+2+2]-cycloaddition[13b–c,20] constructing the main core from simple precursors, tethered dialkynes **1a–b** and "electron-rich" nitriles **2a–c** or α-chloroacetonitrile.

This step involves commercially available $Cp^*Ru(CH_3CN)_3PF_6$ catalyst and makes synthesis divergent in giving the possibility to employ various dialkyne and nitrile precursors that would deliver a library of differentially decorated core building blocks such as 2-aminopyridines and 2-aminomethylenedihydro-pyrrolo-[3,2]-pyridines for the final functionalization.

We selected 2 tethered dialkynes, *N-tert*-butoxycarbonyl-protected propargylic alkyne **1a** and the malonate-derived one **1b**, to couple them with a set of cyanamides **2a–c** (Figure S1 in the Supporting Information) in the presence of the ruthenium catalyst. The first set of 2-amino-pyridines **3a–f** was isolated in 76–96% yields after the cyclization step and in 82–99% yields after the deprotection step (where applicable; Scheme 1, Strategy A). In the second, more general strategy, avoiding the preparation of the individual cyanamides, the α-chloroacetonitrile **4'** was chosen for the subsequent analogs synthesis (Scheme 1, Strategy B), and was prepared starting from compound **1a** in the presence of $Cp^*Ru(CH_3CN)_3PF_6$ catalyst. This key chlorinated derivative was further substituted using a variety of nucleophiles (compounds **5a–x**; Figure S2). The selection of the nucleophiles was based on chemical diversity and drug-likeness considerations and led to the inclusion of anilines with solubility-aiding and fluorine-containing substituents (as in **4a–b,d–i–k–o**), heterocycles, often featuring in RNA binders (as in **4c,j,p–r**) and of secondary aliphatic amines, such as pyrrolidine, dimethylamine, morpholine, piperidine, and piperazine (as in **4s–w**, respectively). Benzylamine (as in **4m**) was further added to probe the optimal length between the aromatic rings and a thiophenol (as in **4x**) replacement was included, as sulfur was recently reported to engage in similar molecular interactions as nitrogen does.[21] The substitution step was optimized by swapping the DMF for acetonitrile as a more sustainable solvent option[22] and conducting the reaction at room temperature in presence of the catalytic amount of KI. The final Boc-deprotection step was conducted with TFA in DCM, with the addition of TES for scavenging the *tert*-butyl cation formed during the reaction.

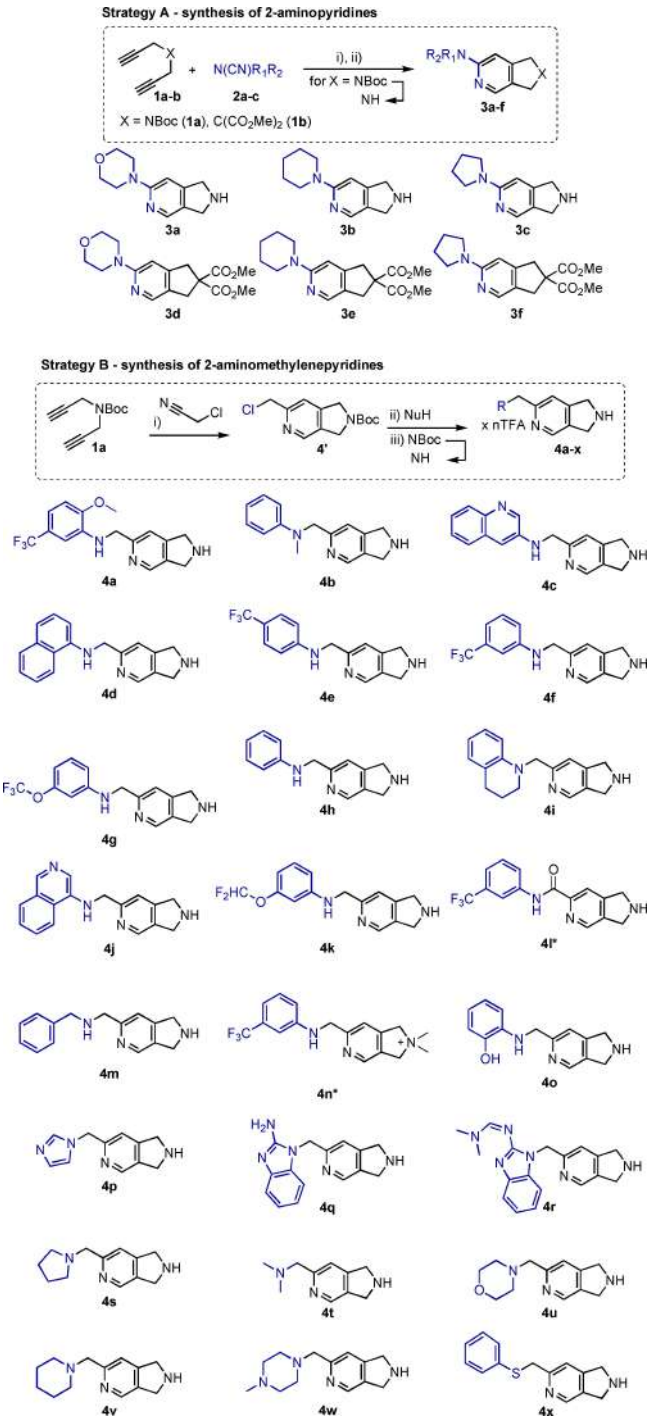

Scheme 1. Strategy A: i) $Cp^*Ru(CH_3CN)_3PF_6$, 2 mol %, DCE, 80 °C, 76–96%; ii) 5 equiv. TFA, DCM, 12 h, RT, 82–99%. Strategy B: i) $Cp^*Ru(CH_3CN)_3PF_6$, 2 mol %, DCE, 80 °C, 86%, ii) 1.3 equiv. K_2CO_3, 0.2 KI, 1.3 equiv. nucleophile, acetonitrile, RT, yield 31–99%, iii) 5 equiv. TFA, 2 equiv. TES, DCM, yield 29–98%; For the modified synthesis of **4l** and **4n**, see the Supporting Information.

Lastly, the methylated pyrrolidine and rigid amide in place of benzylic amine group analogs were synthesized. The pyrrolidine ring was methylated (**4n**) to probe the potential importance of this HBD/HBA. The benzylic position derived

from the nitrile was swapped for the amide link to test the influence of the rigidification on the scaffold (**4l**). For this purpose, the cyanochloroformate was used in place of chloroacetonitrile in [2+2+2]-cycloaddition with the subsequent hydrolysis of the pyridine ester to the acid, which was coupled with an amine. (See the Supporting Information for synthetic details.)

This original and efficient synthetic pathway allowed us to access 30 new and original compounds as unprecedented potential RNA binders. After full characterization of these compounds, we thus moved to the biochemical evaluation of their affinity and activity on pre-miR-21 Dicer processing.

Biochemical evaluation of binding, selectivity and inhibition activity of the synthesized compounds

First, we evaluated the binding of the compounds to the pre-miR-21. The assay we employed uses the 72-mer sequence 5′-labeled with a fluorescent dye and relies on the change in the fluorescence yield upon binding of the ligand to the pre-miR and subsequent modification of the fluorophore environment. We were delighted to see that our de-novo ligand design resulted in some micromolar binders (Tables 1 and S3). Among the first set of compounds **3a**–**f**, only two aliphatic amine analogs have K_D lower than 10 μM, in particular, 7.9±0.1 μM for **3a** and 3.2±0.7 μM for **3b** containing the morpholine and piperidine substitution, respectively. Compound **3c** has a K_D higher than 10 μM, while compounds **3d**–**f** did not show any affinity and they were consequently not included in Table 1. Among the second set of compounds **4a**–**x**, eleven (**4a**–**h,j,k** and **n**) have K_D values under 10 μM and compounds **4a,b,c,f** and **j** bearing the aniline substitution subgroup show K_D lower than 2 μM highlighting the important role of the aniline moiety in binding.

All compounds were then tested for their selectivity in binding pre-miR-21 in presence of a large excess (100 equiv.) of competitors such as duplex DNA and tRNA that represent abundant intracellular potential off-targets. Most of the compounds had shown only a small two- to threefold loss in affinity, yet proving the preference for the pre-miR-21 binding over other nucleic acid structures (Table S1). Finally, the best binders, with K_D values below 10 μM, were selected to evaluate their ability to inhibit the Dicer processing of pre-miR-21. For this assay, we employed a double-labeled pre-miR-21 containing a fluorophore (fluorescein) at the 5′-end and a quencher (Dabcyl) at the 3′-end. When Dicer cleaves the pre-miR-21, the fluorescence signal will thus increase, while in the presence of an efficient inhibitor, no fluorescence change would be detected. Among the best binders, eight were able to inhibit Dicer cleavage with activities spanning from 43.0±3.0 for **4c** and 57±5 for **4a** to 283±36 μM for **4f** (Figure 2, Table S2). Compounds **3b**, **4b**, **4g**, **4k**, and **4n** did not show activity.

The aniline substitution proved to be particularly favorable for inhibition since it was present in seven out of the eight inhibitors. while the morpholine substituent was present in the remaining inhibitor from the aliphatic-substitution group. On the aniline part, the presence of the hydrogen on the aniline is crucial for the activity (no inhibition was observed for the compound **4b**) and CF_3-group in *m*-/*p*-position as in compounds **4a, 4f** and **4e** seems optimal for interaction and inhibition (yet analogous *m*-CHF_2O-/CF_3O-ligands **4g** and **4k** were not active). Alkylation of the pyrrolidine (as in compound **4n**) abrogated the activity, so did the introduction of the linker between aniline nitrogen and benzene ring as in compound **4m**, change of the aniline nitrogen for sulfur as in **4x**, and amide bond rigidification of the scaffold as in compound **4l**.

We, therefore, selected the two best inhibitors **4a** and **4c** as key candidates for the mechanistic studies and further compared them in terms of predicted pharmacokinetics. We found that **4a** had better pharmacokinetic properties, specifically, second best inhibitor had slightly smaller TPSA (49.84 vs. 46.18 Å^2 for **4c** and **4a** respectively), bigger fraction of Csp^3 atoms (0.18 vs. 0.31)[23a–b] and more hydrogen bond acceptors (3 vs. 6) (properties calculations were conducted using the swissADME service http://www.swissadme.ch, see the Supporting Information for details).

Based on the obtained results, we selected compound **4a**, showing the best affinity, inhibition activity, selectivity, and

Table 1. Dissociation constants for the synthesized compounds toward pre-miR-21 at 37 °C.

ID	K_D [μM][a]	ID	K_D [μM][a]
3a	7.9±0.1	**4i**	15.3±1.8
3b	3.2±0.7	**4j**	2.4±0.8
3c	26.9±1.9	**4k**	7.8±2.4
4a	1.9±0.1	**4l**	21.7±1.9
4b	1.6±0.5	**4m**	46.5±0.9
4c	1.9±0.1	**4n**	5.8±0.4
4d	6.4±1.7	**4o**	83±10
4e	2.7±0.4	**4p**	109.7[b]
4f	1.6±0.2	**4q**	49.4±1.5
4g	4.9±1.4	**4r**	28.8±3.2
4h	9.1±1	**4s**	32.5[b]

[a] Binding studies were performed on 5′-FAM-pre-miR-21 in buffer A (20 mm Tris·HCl (pH 7.4), 12 mm NaCl, 2.5 mm $MgCl_2$, and 1 mm DTT). [b] K_D values for compounds **4p** and **4s** were measured once, and the error is estimated at ±10%.

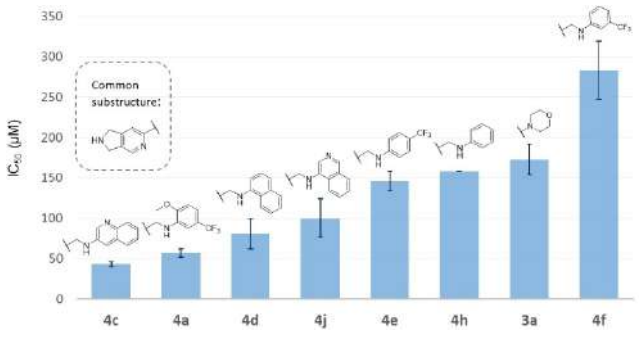

Figure 2. Inhibition activities (IC_{50}, μM) of compounds **4c, 4a, 4d, 4j, 4e, 3b, 4f** and **4b** against pre-miR-21. The assay was performed on 5′-FAM-pre-miR-21-3′-DAB in buffer A (20 mm Tris·HCl (pH 7.4), 12 mm NaCl, 2.5 mm $MgCl_2$, and 1 mm DTT) at 37 °C with human recombinant Dicer.

pharmacological properties to study more in detail the mechanism of interaction with pre-miR-21.

Evaluation of binding site and Dicer inhibition using enzymatic footprinting

To perform a detailed mechanism elucidation, we first conducted the Dicer cleavage experiment in the presence of TARBP, an auxiliary protein involved in Dicer processing of the microRNAs and we analyzed the results by denaturing gel electrophoresis. The incubation of pre-miR-21, whose primary and secondary structure are shown in Figure S4a, with compound **4a** and subsequent addition of the TARBP:Dicer complex had shown a concentration-dependent inhibition of pre-miR-21 cleavage located at G28-A29 residues (Figure S4b). To infer more information on the putative binding site, we also conducted footprinting experiments in the presence of RNase ONE, a ribonuclease catalyzing the hydrolysis of RNA (to cyclic nucleotide monophosphate (NMP) intermediates) at the majority of nucleotides.[24] Having a broader range of visible nucleotides for footprinting allowed us to see a more representative picture of where the binding site is likely located (Figure S4c). The band quantitation revealed dose-dependent inhibition of the cleavage at the nucleotides G28-A29 (abrupt inhibition at the highest concentration was also observed for nucleotides G22-A23, although above the IC_{50} value), thus suggesting that **4a** is binding selectively at the cleavage site of Dicer thus inhibiting its processing.

As RNA flexibility does not allow direct conclusions to be drawn from such an experiment as the binding-induced proximal conformational change can be misleading, we decided to apply molecular modeling to confirm these experimental results. Molecular modeling would be useful not only for binding site elucidation but could also guide us in refining the hit molecule and developing a more potent ligand.

Molecular modeling studies

To probe the binding site hypothesis obtained by footprinting, the binding mechanism of **4a** was predicted in silico by means of molecular docking against pre-miR-21 structure. Given the inherent flexibility of the RNA structure, the conformation to be used in docking was assessed by molecular dynamics (MD) simulations, identifying the most representative structure, in terms of population. Docking on pre-miR-21 structural model showed a significant preference of active ligands over non-active ones in binding to two separate sites (involving the stem and loop regions, near G18 and U43 residues, respectively) that were further investigated by molecular dynamics (MD) simulation. MD trajectories analysis revealed significant stability differences between the two poses, the pose on the loop had lower RMSD values (30.8 ± 9.3 vs. 32.4 ± 12.8 Å, elevated values in both cases are expected due to the flexibility of the microRNA, Figure 3a).

Hydrogen bonding analysis also showed higher relative interacting times of the first (loop) pose (77%) compared to the second (stem) (63%), which could also indicate higher stability, as shown in Figure 3b (left and right panels, respectively). Visual inspection of the trajectory obtained from the first docking pose revealed that the main binding mode is given through a steady anchoring of the pyrrolidinic nitrogen between ligand and receptor and a parallel conformation to the pre-miR. Cluster analysis of the simulation led to the identification of three main states, with one being predominant over most of the simulation time (Figure 3c) This pose was then used as a reference for comparison with the experimental results obtained in the laboratory.

Epitope mapping by STD NMR

Finally, we decided to couple the STD NMR with molecular docking and MD simulation to find the concurrent hints on the mode and site of interaction. The low micromolar affinity value is an ideal point to engage this type of NMR experiment, as the complex formation should be sufficiently "loose" and the ligand residence time in a complex should allow some of the bound ligand to be released back into solution within the timescale of the measurement.[25a–b] In conducting the multifrequency measurements, we wanted to adopt a differential STD NMR procedure, largely known for proteins, that can be very useful when juxtaposing the data with docking poses. Moreover, the lower proton density of RNA compared to that of the proteins could help to make the difference more pronounced, as was showcased in the literature.[25c] Thus, acquiring the data after irradiation at 4.1, 5.7 and 7.8 ppm, we would observe the saturation transfer from the sugar backbone; non-exchangeable protons at C5 of the uridine and cytosine (pyrimidine bases), C1 of the sugar ring; and C8 guanine and adenine (purine bases), C6 uridine and cytosine, C2 adenine respectively (the data was taken from the available NMR assignment for the pre-miR-21 pre-element; Figure 4a).[26]

The plotted intensities observed for compound **4a** for each ligand proton (Figure 4b) directly reflect their physical proximity to the biomolecule (different colors refer to different irradiation frequencies). To our delight, the relative acquired STD NMR signal intensities of the ligand protons correlated well with their physical proximity to pre-miR-21 in the complex after MD simulation. The benzylic protons' analysis was omitted since they overlapped with the water signal. Overall, the pyridine *meta*-positioned proton (ε, Figure 4c) had shown the biggest STD intensities, hence it is closest to the pre-miRNA in the complex. It has also shown more saturation transfer from the aromatic non-exchangeable protons, than from the sugar backbone. This was rather surprising given that most of the dockings showed repeated interaction of the benzylic nitrogen with the sugar backbone, which would place the pyridine protons not too far from it. Vicinal aniline protons followed (γ-δ, Figure 4c), on the contrary with higher saturation transferred from the sugar backbone. The *ortho*-pyridine proton (ζ, Figure 4c) showed slightly lower intensity, with yet greater

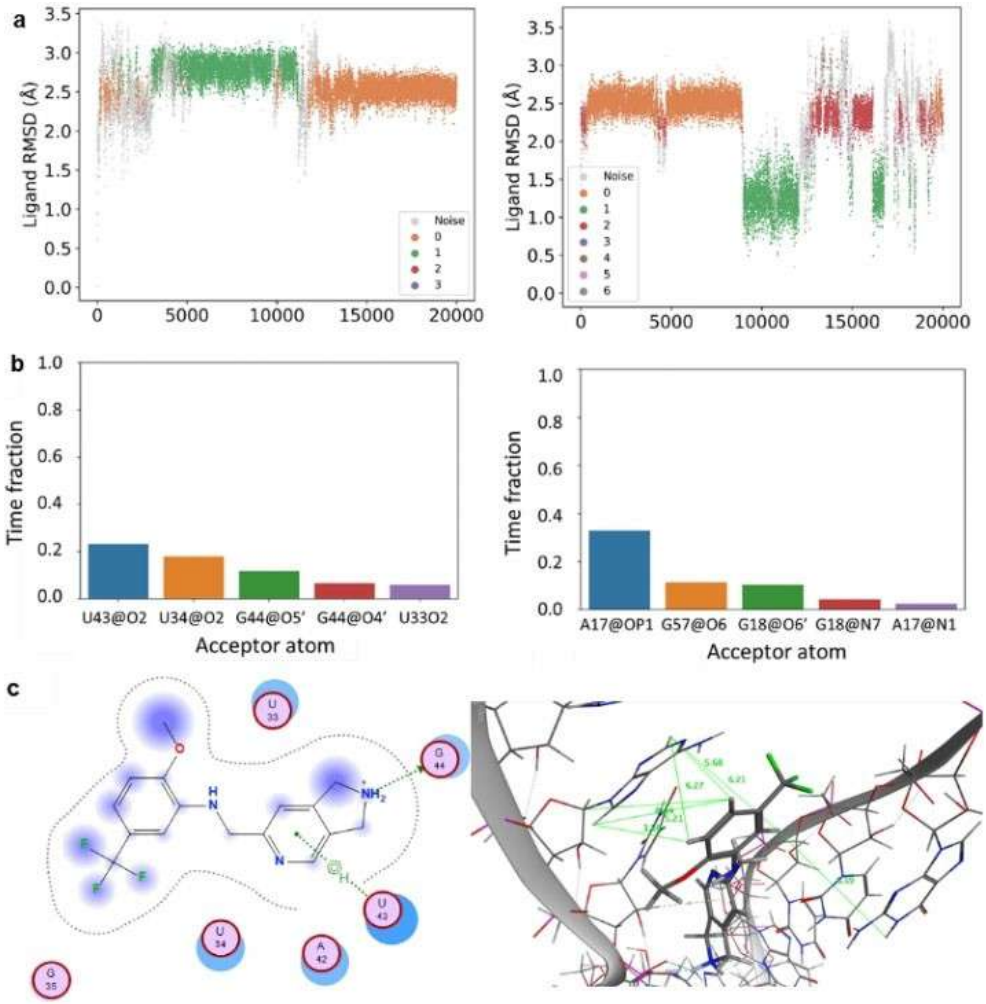

Figure 3. Molecular dynamics simulations and docking. a) Ligand (**4a**) RMSD during simulation trajectory, colored by cluster analysis. Results are shown for the two main interaction sites identified in docking: the U43 region (left) and G18 region (right). b) Relative times vs nucleotides involved in the interaction with **4a** (poses U43 and G18 from left to right). c) Molecular representation of the most probable interaction mechanism between **4a** and pre-miR-21 model found: measured distances between ligand hydrogens and receptor (left), mapped interaction legend, size of the purple radii correlates with the physical proximity (right).

importance of the sugar saturation transfer. The isolated aniline proton (β, Figure 4c) closed the aromatic protons rank, and the methoxy group (α, Figure 4c) was preferentially saturated at 5.7 ppm.

The absence of the rigid pockets on the RNA puts fewer constraints on the solid "black and white" mode of binding, leaving room for discrepancies in the models coming from the different experiments. These results taken together with modeling studies indicate the high involvement of the dihydropyrrole nitrogen of **4a** in the hydrogen-bond interaction with G44 and pyridine ring anchored by an accepting H-bond from U43. The aniline moiety likely provides a well-positioned hydrophobic consolation to A42 and U43 nucleobases while not intercalating. Close inspection of the pose suggests several sites for further modification of the compounds in view of optimization of the biological activity, namely, ortho-vector on the aniline ring, free ortho-position of the pyridine and dihydropyrrole nitrogen with preservation of its ability to engage in H-bonding.

Conclusion

In conclusion, we have synthesized an RNA-focused library targeted against the production of the oncogenic microRNA-21, and discovered 2-amino-dihydropyrrolo-[3,2]-pyridine and 2-aminomethylene-dihydropyrrolo-[3,2]-pyridine as new and original scaffolds for RNA binding. The synthesis was designed and optimized to deliver the compounds in five steps in good yields by employing sustainable chemistry. Five compounds have low-micromolar affinities towards pre-miR-21, good selectivity against other nucleic acid structures, and promising inhibition activity on the Dicer processing of the pre-miR-21 in the two-digit micromolar range. The mechanism of action was studied in depth by enzymatic footprinting and molecular modeling

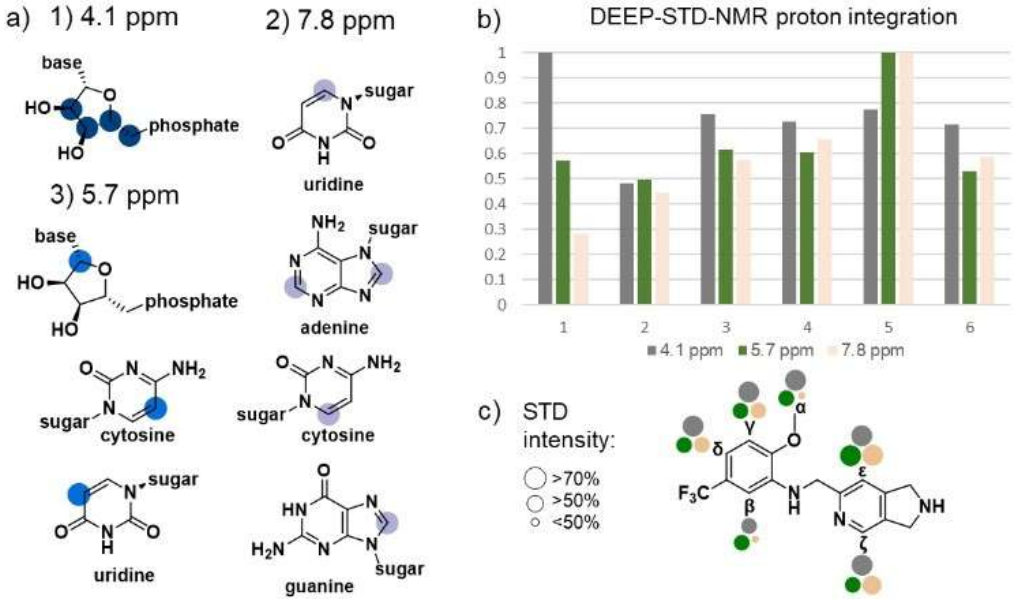

Figure 4. Differential-frequency saturation transfer difference (DEEP-STD) NMR. a) Differential irradiation frequencies; b) interaction intensity histogram (*y*-axis) of different ligand **4a** protons (*x*-axis); c) epitope mapping of ligand **4a**. Samples for the STD NMR study were prepared in buffer C, a phosphate buffer containing 75 μM $Na_2HPO_4 \cdot 7H_2O$, 25 μM $KH_2PO_4 \cdot H_2O$ and 2.5 mM $MgCl_2$ in D_2O, pH 7.4, an additional amount of [D_6]DMSO $\leq$ 10% was used to aid the solubility of the ligand. The ratio of the ligand to pre-miR-21 was 1000:1, with the final ligand concentration 1 mM.

and allowed us to confirm that the trifluoromethylaniline derivative is an efficient binder of the cleavage site of Dicer on the pre-miR-21 sequence. STD NMR allowed us to identify the parts of the most active compound that bind the target; great agreement with the molecular modeling study was shown. Altogether, the results allowed us to establish unprecedented structure–activity relationships and identify the most promising modifications that could be introduced in the future for ligand optimization that is currently ongoing.

Methods

RNA and biochemicals: All buffers and solutions employed in FRET assays, K_D measurements and footprint experiments were filtered through 0.22 μm Millipore filters (GP ExpressPLUS membrane).

RNA and DNA oligonucleotides were purchased from Eurogentec (Belgium). A mixture of yeast pre- and mature tRNAs (containing > 30 different species) was purchased from Sigma (type X-SA). A buffer A used in the FRET assays, K_D determination, and RNases footprint experiments is a buffer containing 20 mm Tris·HCl (pH 7.4), 12 mm NaCl, 2.5 mm $MgCl_2$, and 1 mm DTT. A buffer B used in gel electrophoresis experiment is a 1x TBE buffer containing 50 mM Tris base, 55 mM boric acid, 1 mM EDTA. A buffer C used in STD NMR study is a phosphate buffer containing 75 μM $Na_2HPO_4 \cdot 7(H_2O)$, 25 μM $KH_2PO_4 \cdot H_2O$ and 2.5 mM $MgCl_2$ in D_2O, pH 7.4, an additional amount of [D_6]DMSO $\leq$ 10% was used to aid the solubility of the ligand.

RNase T1 was purchased from Ambion (1 U/μL), RNase ONE from Promega (10 U/μL), human recombinant Dicer enzyme from BioCat GmbH (0.05 μg/μL) and TARBP2 protein from BioCat GmbH (1 mg/mL).

Oligonucleotides: Pre-miR-21 used sequence: 5′-UGUCGGGUAGCUUAUCAGACUGAUGUUGACUGUUGAAUCUCAUGGCAACACCAGUCGAUGGGCUGUCUGACA-3′.

DNA duplex sequence: 5′-CGTTTTTATTTTTGC-3′.

Fluorescence-based assays: The FRET-Dicer assay and K_D determinations were performed in 384-well black plates (Greiner bio-one) in a final volume of 40 μL using a 5070 EpMotion automated pipetting system (Eppendorf). Each experiment was performed in duplicates and repeated three times. Refolding of the RNA was performed using a thermocycler (ThermoStatPlus Eppendorf) as follows: the RNA (5′-FAM-pre-miR-21-3′-DAB for FRET experiments and 5′-FAM-pre-miR-21 for K_D measurements), diluted in 1 mL of buffer A, was first denatured by heating to 90 °C for 2 min and then cooled to 4 °C for 10 min, followed by incubation at 25 °C for 20 min. After refolding, the RNA was diluted to a working concentration of 50 nM (for FRET-Dicer assays) or 10 nM (for binding assays) through the addition of the appropriate amount of buffer A. During FRET-Dicer assay, 10 μL of pre-miR-21 beacon solution were added in each well containing 5 μL of each desired ligand concentration (from 488 nM to 1 mM). These reaction mixtures were pre-incubated at room temperature for 30 min. 0.25 U of human recombinant Dicer (BioCat GmbH) and 0.25 U of TARBP2 protein (BioCat GmbH) in 5 μL were then added (final volume 20 μL) and the plate was incubated at 37 °C for 20 hours. During binding assays, 30 μL of pre-miR-21 beacon solution were added in each well containing 30 μL of each desired ligand concentration (final volume 60 μL). Each ligand was added in 15 dilutions (from 61 nM to 1 mM) and fluorescence was measured

after incubating the plate at 4 °C overnight. The fluorescence was measured on a GeniosPro (Tecan) with an excitation filter of 485 ± 10 nm and an emission filter of 535 ± 15 nm. Each point was measured 10 times with a 500 μs integration time and averaged. Inhibition data were analyzed using GraphPad Prism 5 software using a nonlinear regression following the equation: $Y = \text{Bottom} + (\text{Top} - \text{Bottom})/1 + 10^{[(\log IC_{50} - X) \times \text{Hills slope}]}$). Binding profiles were well modeled using a simple model assuming a one-to-one stoichiometry. In competition experiments, the RNA beacon was first mixed with 100 equiv. of tRNA mix or DNA duplex.

RNase footprinting assays: 0.2 nmol of 5′-FAM-pre-miR-21 were diluted in 100 μL of buffer A (final concentration 1 nM), were first denatured by heating to 90 °C for 2 min and then cooled to 4 °C for 10 min, followed by incubation at 25 °C for 15 min. One microliter of RNase T1 (concentration = 0.033 U/μL) and RNase ONE (concentration = 0.002 U/μL) was added to the RNA beacon preincubated in the absence or in the presence of compound **4a** at 4 °C overnight (final reaction volume 10 μL). The reaction was incubated 15 min at 37 °C and stopped by ethanol precipitation (100 μL). Two microliters of human recombinant Dicer (0.5 U/μL, BioCat GmbH) were added to the RNA beacon preincubated in the absence or in the presence of compound **4a** at 4 °C overnight (final reaction volume 10 μL). The reaction was incubated 1 h at 37 °C and stopped by ethanol precipitation (100 μL). The alkaline hydrolysis reagent containing 26.5 mg Na_2CO_3, 1 μL EDTA 0.5 M in 5 mL H_2O was diluted 3 times and 5 μL of the final solution was added to the 5 μL of pre-miR-21. The reaction was incubated for 2 min at 90 °C and stopped by ethanol precipitation (100 μL). All footprinting samples were resuspended in 95% formamide and heated at 90 °C for 2 min before being loaded onto a denaturing 20% polyacrylamide (19:1 acrylamide/bisacrylamide) containing 7.5 M urea in buffer B. Gels were scanned with a Versadoc (Biorad) at 480 nm.

STD NMR: All RNA/ligand samples were prepared in a 1000:1 ligand/RNA ratio in buffer C. The final concentration of the samples was 1000 μM of ligand **4a** and 1 μM of pre-miR-21, and the final volume was 400 μL.

High-resolution NMR experiments were recorded on a BRUKER AVANCE NEO Ultra shield DRX 500 spectrometer operating at 500.13 MHz for ^{1}H, equipped with a temperature control unit (BCU I, B-SVT), and a 5 mm PADUAL ^{13}C,^{1}H Z-Grad probe. Chemical shifts (δ) are expressed in parts per million (ppm). DMSO signal (2.71 ppm) was used as a chemical shift reference. All NMR experiments were carried out using standard pulse sequences supplied by the spectrometer manufacturer (Bruker). The probe temperature was maintained at 15 °C. All spectra were analyzed using Mnova 12.0 software. Intensities of STD effects (absolute STD) were calculated by dividing the integral values of each proton in STD spectra by the respective integral values from the reference spectrum.

STD NMR experiments were carried out at 300 K using stddiff pulse sequence. ^{1}H STD NMR spectra were recorded alternating "on" (4.1, 5.7 or 7.8 ppm) and "off" (−40 ppm) resonance saturation. Each proton NMR spectrum was acquired using 7812.5 Hz spectral width (SW), center was set at 2350.61 Hz (4.7 ppm), 64 K complex data point (TD), acquisition time (aq) of 4.19 s, relaxation delay (D1) of 2 s, number of scans (ns) between 120 and 512, number of dummy scans (ds) 16 and a 90° flip angle pulse width. Selective saturation was achieved using a series of 40 equally spaced 50 ms Gaussian-shaped pulses (Gaus1.1000) and an attenuation of 0.0001 Watt (40 dB) giving a total saturation time of 2 s. To test the shaped pulse selectivity, a STD experiment on ligand alone without RNA present was acquired. No ligand signals were present in the STD spectrum, proving the selectivity of the Gaussian pulse. Subtraction of FID values with on- and off-resonance was achieved by phase cycling sequence. Prior to Fourier transformation an exponential line broadening function of 0.3 Hz was applied and the data zero filled to 64 K.

Docking and molecular dynamics simulations

pre-miRNA-21 structural model: The tertiary structure of pre-miR-21 was predicted using McSym/McFold servers (https://major.iric.ca/MC-Fold/) to fold the sequence retrieved from miRbase (http://www.mirbase.org), applying the constraints needed to maintain the secondary structure. The lower stem of the structure with the lowest energy from a server was used to construct a hybrid model compiled with an apical loop NMR model available from the Protein Data Bank (PDB ID: 5UZT). The structure was neutralized using the tLeap module in AMBER20[27] with sodium and chloride ions and solvated with TIP3P water molecules in a truncated octahedral box. 400 ns of MD simulation were conducted and analysed following the protocol described for the RNA/ligand complex simulations hereafter. Cluster analysis was performed and the prevailing over the course of simulation conformation (cluster 0) was chosen based on this parameter and used further in docking.

*Molecular docking to predict the binding mechanism of **4a***: The binding mechanism of **4a** against the aforementioned pre-miR-21 structural model was predicted by molecular docking. Blind docking was performed using MOE 2020.09[28] under induced fit conditions using amber14:EHT force field. London dG score function was used on the initial placement stage and 200 poses were collected for each ligand which were further refined with GBVI/WSA dG score function retaining the best 100 poses. The resulting database was analyzed with PLIF MOE tool[29] to find the commonality in the interactions made by active ligands.

Molecular dynamics simulations: The corresponding complexes of RNA and **4a** bound in both sites were extracted and were then further prepared using the tLEaP module included in the Amber20 Molecular Dynamics (MD) software[27] considering the AMBER*ff99OL3* force field[29] with the backbone phosphate modifications.[30] The systems were neutralized and solvated with the OPC water model[31] defining a 10 Å radius solvent box before proceeding to MD simulations.

Simulations were computed with the SANDER and PMEMD modules using the SHAKE algorithm to constrain all bonds involving hydrogens at all stages and employ an 8 Å cutoff for nonbonded interactions.

Two initial minimization stages were performed with PMEMD defining a 9 Å cutoff for long-range interactions. No bond constraints were applied. Each stage consisted of a total of 5000 steps using Steepest Descent method (switched to Conjugate Gradient after the first 1500 steps). The first stage included a 2.0 kcal/mol positional restraint on the RNA model to avoid solute distortion while minimizing the solvent, followed by the second stage, which did not include any restraint. The system was then heated for 0.5 ns to 300 K using the Langevin thermostat in a canonical NVT collective and 0.002 ps time step. A density stage was carried out in NPT conditions to allow stabilization of the density of the system, followed by a preproduction stage (0.5 ns each) to let the whole system equilibrate. Finally, a 200 ns production stage was conducted under the NPT collective. The heating, density, equilibration, and production stages were performed by applying the SHAKE algorithm to constrain all bonds concerning hydrogen atoms.

The resulting trajectories were analyzed using cpptraj[29] to perform a basic analysis of the systems, including microRNA and ligand RMSD and hydrogen bonding analysis. The trajectories were also clustered using the DBScan method[32] in order to obtain representative structures of the binding modes sampled by MD. Clustering parameters were iteratively adjusted as recommended in the AMBER manual[27] by first generating a "K-Dist" plot to select the minpoints value and then performing several runs while varying epsilon ε. Clusters with peak pseudo-F statistic (pSF) and lowest Davies – Bouldin Index (DBI) values,[33] were selected as the best clusters, and were further examined to avoid the presence of singletons and equally sized clusters (which tend to give low DBI and higher pSF values, respectively).

The centroid of the biggest clusters with a stable ligand RMSD were selected to display the representative binding modes on each site.

Experimental Section

Materials: Reagents and solvents were purchased from Merck and Carlo Erba Reagents and used without further purification. All reactions involving air- or moisture-sensitive reagents or intermediates were performed under an argon atmosphere. Flash column chromatography was carried out on silica gel columns (Interchim Puriflash silica HP 15 μm) on a Puriflash XS420 system (Interchim). The purification of final compounds salts was carried out by hydrophilic interaction liquid chromatography (HILIC) with a gradient of CH_3CN containing 0.5% TFA (eluent B) and water containing 0.5% TFA from 0 to 20% of B on normal phase silica gel columns (Interchim Puriflash silica HP 15 μm). Analytical thin-layer chromatography (TLC) was conducted on Sigma–Aldrich precoated silica gel and compounds were visualized by irradiation (254 nm) and/or by staining with potassium permanganate. HPLC was performed using a Waters ARC UHPLC pump coupled to a Waters 2998 photodiode array detector and Waters Cortex® $C_{18}+$ column (50×4.6 mm, 2.7 μm). Analyses were run at room temperature by using a gradient of CH_3CN containing 0.1% TFA (eluent B) in water containing 0.1% TFA (eluent A) at a flow rate of 1.5 mL min^{-1}. ^1H and ^{13}C NMR spectra were recorded on a Bruker AC 200 MHz or a Bruker AC 400 MHz spectrometer. Chemical shifts are reported in parts per million (ppm, δ) referenced to the residual ^1H resonance of the solvent ($CDCl_3$, δ 7.26; [D_4]methanol, δ 3.31; D_2O δ 4.79, [D_4]acetonitrile, δ 1.94). Splitting patterns are designated as follows: s (singlet), d (doublet), t (triplet), m (multiplet), br (broad). Used abbreviations: DCM (dichloromethane), TEA (triethylamine), PE (petroleum ether). Coupling constants (*J* values) are listed in hertz (Hz). High-resolution mass spectroscopy (HRMS) of the new compounds was performed by Institut de Chimie de Nice using a Thermo Vanquish UHPLC instrument coupled with a Thermo Q-Exactive (UPLC-HRMS) Orbitrap (Thermo Fisher Scientific GmbH, Bremen, Germany) and an ESI source operated with the Xcalibur (version 2.2, ThermoFisher Scientific) software package. The number of the contranions for the final compounds (representative of different structural subgroups in the library) after acid-catalyzed deprotection were determined by ^{19}F NMR.

Synthesis: Cyanamide compounds (Figure S1) were prepared following a published procedure[34] and using *t*BuOK as a base with the corresponding yields of 44, 68 and 46%.

***N*-Boc-dipropargyl amine (1 a)**: was prepared in two steps following the published procedures (in quantitative and 91% yields for the two subsequent steps, spectral data in accordance with the literature).[35a–b]

2,2-Di(prop-2-ynyl)-malonic acid dimethyl ester (1 b): was prepared following the published procedure (79% yields, spectral data in accordance with the literature).[36]

***tert*-Butyl 6-(chloromethyl)-1,3-dihydro-*2H*-pyrrolo[3,4-c]pyridine-2-carboxylate (4′)**: $Cp^*Ru(CH_3CN)_3PF_6$ (2 mol%, 55 mg, 0.1 mmol), diyne (1 equiv., 1 g, 5.17 mmol), and chloroacetonitrile (2 equiv, 0.78 g, 10.3 mmol) were heated at 70 °C in a tube with septum and parafilm in dichloroethane (10 mL) and under argon. After 18 h, the reaction mixture was concentrated under the reduced pressure. The crude product was purified by column chromatography (PE/EtOAc/TEA (80/19/1)) to give 1.2 g of the product as white solid, 87% yield. Spectra correspond to those reported.[37] ^1H NMR (200 MHz, $CDCl_3$): δ = 8.47 (s, 1H), 7.38 (s, 1H), 4.73-4.63 (m, 6H), 1.50 ppm (s, 9H). ^{13}C NMR (50 MHz, $CDCl_3$): δ = 155.6, 154.3, 148.0, 144.0, 133.2, 117.2, 80.4, 51.8, 50.1, 46.7, 28.5 ppm.

General procedure for [2+2+2]-cyclization with cyanamide (procedure A): $Cp^*Ru(CH_3CN)_3PF_6$ (3 mol %, 15 mg, 0.028 mmol), diynes **1 a** (180 mg) or **1 b** (194 mg), 1 equiv., 0.932 mmol), and cyanamide (**2 a–c**, 1 equiv., 0.932 mmol, 0.932 mL of 1 M stock solution in dichloroethane (DCE)) were stirred at 70 °C in a screw-capped tube in DCE (10 mL total) under argon. The reaction completion was detected by TLC (24 h, potassium permanganate staining). The mixture was cooled down to room temperature, concentrated under reduced pressure and deposited onto a silica pad. This latter was washed with petroleum ether (30 mL) and the pyridine compound was eluted with EtOAc (10 mL). The collected EtOAc fraction was concentrated under the reduced pressure to deliver the cyclized products **3 a–c**.

General procedure for amine substitution (procedure B): The screw-capped tube was charged with *tert*-butyl 6-(chloromethyl)-1,3-dihydro-*2H*-pyrrolo[3,4-c]pyridine-2-carboxylate (**4′**, 75 mg, 0.28 mmol, 1 equiv.), K_2CO_3 (65 mg, 0.36 mmol, 1.3 equiv.), KI (10 mg, 0.06 mmol, 0.2 eq) and the nucleophile reagent (**5 a–x**, Figure S2, numbers correspond to the substitution product; 0.33 mmol, 1.2 equiv.) in CH_3CN (1 mL) and the reaction mixture was stirred at room temperature. After 24 h, the reaction mixture was concentrated under reduced pressure and diluted with water (5 mL). The aqueous layer was extracted with EtOAc (3 times 5 mL), the organic phase dried over $MgSO_4$ and finally concentrated under the reduced pressure. The crude product was purified by column

chromatography (PE/EtOAc/TEA (65/34/1)) to separate the excess of the nucleophile and subsequently used in the deprotection step.

General procedures for Boc deprotection (procedure C): In a round-bottomed flask charged with a magnetic stirring bar the Boc-protected amines (1 equiv., 0.11 mmol) was dissolved in the DCM (0.5 mL) and TES (25 mg, 0.22 mmol, 2 equiv.) was added. The reaction mixture was cooled down to 0 °C and TFA (126 mg, 0.085 mL, 1.1 mmol, 10 equiv.) was added dropwise. The reaction mixture was warmed up to room temperature and was kept stirring for 18 h. After the reaction completion was detected by TLC, the mixture was concentrated under reduced pressure and purified by hydrophilic column chromatography leading to desired compounds.

General procedures for Boc deprotection (procedure D): To the Boc-protected amines (1 equiv., 0.1 mmol in 2 mL dioxane) 0.125 mL of HCl (5 equiv., 4 M in dioxane) was added. The reaction was stirred at the room temperature until the completion was detected by TLC (18 h). The precipitate was filtrated, washed with the Et_2O and dried under reduced pressure to deliver the desired compounds.

Acknowledgements

This research received funding from the French government through the UCAJEDI Investments in the Future project with the reference number ANR-15-IDEX-01, Region PACA and BoostUrCareer project European Union's Horizon 2020 research and innovation program under grant agreement no. 847581. M.A. and V.M. also acknowledge Université Côte d'Azur and Centre National de la Recherche Scientifique (CNRS). This study was partly supported by research funding from the Canceropôle PACA, Institut National du Cancer and Région Sud. We are grateful to Dr Marc Gaysinski (Université Côte d'Azur) for help with the STD NMR.

Conflict of Interests

The authors declare no conflict of interest.

Data Availability Statement

The data that support the findings of this study are available from the corresponding author upon reasonable request.

Keywords: binding mechanisms · drug discovery · inhibitors · oncogenes · RNA

[1] J. L. Childs-Disney, X. Yang, Q. M. R. Gibaut, Y. Tong, R. T. Batey, M. D. Disney, *Nat. Rev. Drug Discovery* **2022**, *21*, 736–762.
[2] D. N. Wilson, *Nat. Rev. Microbiol.* **2014**, *12*, 35–48.
[3] H. Ratni, M. Ebeling, J. Baird, S. Bendels, J. Bylund, K. S. Chen, N. Denk, Z. Feng, L. Green, M. Guerard, P. Jablonski, B. Jacobsen, O. Khwaja, H. Kletzl, C.-P. Ko, S. Kustermann, A. Marquet, F. Metzger, B. Mueller, N. A. Naryshkin, S. V. Paushkin, E. Pinard, A. Poirier, M. Reutlinger, M. Weetall, A. Zeller, X. Zhao, L. Mueller, *J. Med. Chem.* **2018**, *61*, 6501–6517.
[4] J. P. Falese, A. Donlic, A. E. Hargrove, *Chem. Soc. Rev.* **2021**, *50*, 2224–2243.
[5] S. T. Crooke, B. F. Baker, R. M. Crooke, X. Liang, *Nat. Rev. Drug Discovery* **2021**, *20*, 427–453.
[6] K. D. Warner, C. E. Hajdin, K. M. Weeks, *Nat. Rev. Drug Discovery* **2018**, *17*, 547–558.
[7] M. Winkle, S. M. El-Daly, M. Fabbri, G. A. Calin, *Nat. Rev. Drug Discovery* **2021**, *20*, 629–651.
[8] S. Volinia, G. A. Calin, C.-G. Liu, S. Ambs, A. Cimmino, F. Petrocca, R. Visone, M. Iorio, C. Roldo, M. Ferracin, R. L. Prueitt, N. Yanaihara, G. Lanza, A. Scarpa, A. Vecchione, M. Negrini, C. C. Harris, C. M. Croce, *Proc. Natl. Acad. Sci. USA* **2006**, *103*, 2257–2261.
[9] a) H. Yin, G. Xiong, S. Guo, C. Xu, R. Xu, P. Guo, D. Shu, *Mol. Ther.* **2019**, *27*, 1252–1261; b) L. X. Yan, Q. N. Wu, Y. Zhang, Y. Y. Li, D. Z. Liao, J. H. Hou, J. Fu, M. S. Zeng, J. P. Yun, Q. L. Wu, Y. X. Zeng, J. Y. Shao, *Breast Cancer Res.* **2011**, *13*, R2; c) M. Y. Shah, A. Ferrajoli, A. K. Sood, G. Lopez-Berestein, G. A. Calin, *EBioMedicine* **2016**, *12*, 34–42; d) S. H. Javanmard, G. Vaseghi, A. Ghasemi, L. Rafiee, G. A. Ferns, H. N. Esfahani, R. Nedaeinia, *Cancer Cell Int.* **2020**, *20*, 38; e) D. Bhere, N. Arghiani, E. R. Lechtich, Y. Yao, S. Alsaab, F. Bei, M. M. Matin, K. Shah, *Sci. Rep.* **2020**, *10*, 1779; f) A. Ghosh, N. Ranjan, L. Jiang, A. H. Ansari, N. Degyatoreva, S. Ahluwalia, D. P. Arya, S. Maiti, *Mol. Ther. Nucleic Acids* **2022**, *27*, 685–698.
[10] a) B. Lahooti, S. Poudel, C. M. Mikelis, G. Mattheolabakis, *Front. Oncol.* **2021**, *11*; 705634; b) Y. Li, Y. Chen, J. Li, Z. Zhang, C. Huang, G. Lian, K. Yang, S. Chen, Y. Lin, L. Wang, K. Huang, L. Zeng, *Cancer Sci.* **2017**, *108*, 1493–1503; c) C. Gong, Y. Yao, Y. Wang, B. Liu, W. Wu, J. Chen, F. Su, H. Yao, E. Song, *J. Biol. Chem.* **2011**, *286*, 19127–19137; d) M. Mei, Y. Ren, X. Zhou, X. Yuan, L. Han, G. Wang, Z. Jia, P. Pu, C. Kang, Z. Yao, *Technol. Cancer Res. Treat.* **2010**, *9*, 77–86; e) U. K. Sukumar, R. J. C. Bose, M. Malhotra, H. A. Babikir, R. Afjei, E. Robinson, Y. Zeng, E. Chang, F. Habte, R. Sinclair, S. S. Gambhir, T. F. Massoud, R. Paulmurugan, *Biomaterials* **2019**, *218*, 119342.
[11] a) P. Zhang, X. Liu, D. Abegg, T. Tanaka, Y. Tong, R. I. Benhamou, J. Baisden, G. Crynen, S. M. Meyer, M. D. Cameron, A. K. Chatterjee, A. Adibekian, J. L. Childs-Disney, M. D. Disney, *J. Am. Chem. Soc.* **2021**, *143*, 13044–13055; b) J. S. Matarlo, L. R. H. Krumpe, W. F. Heinz, D. Oh, S. R. Shenoy, C. L. Thomas, E. I. Goncharova, S. J. Lockett, B. R. O'Keefe, *Cell Chem. Biol.* **2019**, *26*, 1133–1142.e4; c) S. P. Velagapudi, M. G. Costales, B. R. Vummidi, Y. Nakai, A. J. Angelbello, T. Tran, H. S. Haniff, Y. Matsumoto, Z. F. Wang, A. K. Chatterjee, J. L. Childs-Disney, M. D. Disney, *Cell Chem. Biol.* **2018**, *25*, 1086–1094.e7; d) C. Becquart, M. Le Roch, S. Azoulay, P. Uriac, A. Di Giorgio, M. Duca, *ACS Omega* **2018**, *3*, 16500–16508; e) C. Maucort, D. D. Vo, S. Aouad, C. Charrat, S. Azoulay, A. Di Giorgio, M. Duca, *ACS Med. Chem. Lett.* **2021**, *12*, 899–906.
[12] a) T. P. A. Tran, S. Poulet, M. Pernak, A. Rayar, S. Azoulay, A. Di Giorgio, M. Duca, *RSC Med. Chem.* **2022**, *13*, 311–319; b) D. D. Vo, T. P. A. Tran, C. Staedel, R. Benhida, F. Darfeuille, A. Di Giorgio, M. Duca, *Chem. Eur. J.* **2016**, *22*, 5350–5362.
[13] a) K. P. C. Vollhardt, *Angew. Chem. Int. Ed. Engl.* **1984**, *23*, 539–556; b) F. Ye, M. Haddad, V. Ratovelomanana-Vidal, V. Michelet, *Org. Lett.* **2017**, *19*, 1104–1107; c) F. Ye, M. Haddad, V. Michelet, V. Ratovelomanana-Vidal, *Org. Chem. Front.* **2017**, *4*, 1063–1068; d) H. Chowdhury, A. Goswami *Adv. Synth. Catal.* **2017**, *359*, 314–322; e) D. Bhatt, N. Patel, H. Chowdhury, P. V. Bharatam, A. Goswami *Adv. Synth. Catal.* **2018**, *360*, 1876–1882.
[14] G. Domínguez, J. Pérez-Castells *Chem. Soc. Rev.* **2011**, *40*, 3430–3444 and the references cited therein.
[15] A. L. Garner, D. A. Lorenz, J. Sandoval, E. E. Gallagher, S. A. Kerk, T. Kaur, A. Menon, *ACS Med. Chem. Lett.* **2019**, *10*, 816–821.
[16] K. Gumireddy, D. D. Young, X. Xiong, J. B. Hogenesch, Q. Huang, A. Deiters, *Angew. Chem. Int. Ed.* **2008**, *47*, 7482–7484.
[17] a) N. F. Rizvi, J. J. P. Santa Maria, A. Nahvi, J. Klappenbach, D. J. Klein, P. J. Curran, M. P. Richards, C. Chamberlin, P. Saradjian, J. Burchard, R. Aguilar, J. T. Lee, P. J. Dandliker, G. F. Smith, P. Kutchukian, E. B. Nickbarg, *SLAS Discovery* **2020**, *25*, 384–396; b) B. S. Morgan, J. E. Forte, R. N. Culver, Y. Zhang, A. E. Hargrove, *Angew. Chem. Int. Ed.* **2017**, *56*, 13498–13502.
[18] G. Padroni, N. N. Patwardhan, M. Schapira, A. E. Hargrove, *RSC Med. Chem.* **2020**, *11*, 802–813.
[19] a) A. Carrër, S. Turban, N. Provost, A. Caliez, G. Lamarche, G. Zanirato, M. Beucher, C. Pean, O. Mirguet, F. Perron-Sierra, V. Michelet, *Bioorg. Chem.* **2019**, *92*, 103243–103248; b) V. Michelet, *Chem. Rec.* **2021**, *21*, 3884–3896; c) Y. Tang, I. Benaissa, M. Huynh, L. Vendier, N. Lugan, S. Bastin, P. Belmont, V. César, V. Michelet, *Angew. Chem. Int. Ed. Engl.* **2019**, *58*, 7977–7981.

[20] F. Ye, F. Boukattaya, M. Haddad, V. Ratovelomanana-Vidal, V. Michelet, *New J. Chem.* **2018**, *42*, 3222–3235.
[21] B. R. Beno, K.-S. Yeung, M. D. Bartberger, L. D. Pennington, N. A. Meanwell, *J. Med. Chem.* **2015**, *58*, 4383–4438.
[22] T. Welton, *Proc. Math. Phys. Eng. Sci.* **2015**, *471*, 20150502.
[23] a) F. Lovering, *MedChemComm* **2013**, *4*, 515–519; b) K. E. Prosser, R. W. Stokes, S. M. Cohen, *ACS Med. Chem. Lett.* **2020**, *11*, 1292–1298.
[24] V. Shen, D. Schlessinger in *The Enzymes* (Ed.: P. D. Boyer), Academic Press, New York, **1982**, pp. 501–515.
[25] a) F. Vasile, S. Della Volpe, F. A. Ambrosio, G. Costa, M. Y. Unver, C. Zucal, D. Rossi, E. Martino, A. Provenzani, A. K. H. Hirsch, S. Alcaro, D. Potenza, S. Collina, *Sci. Rep.* **2018**, *8*, 13780; b) J. Angulo, P. M. Nieto, *Eur. Biophys. J.* **2011**, *40*, 1357–1369; c) S. Di Micco, C. Bassarello, G. Bifulco, R. Riccio, L. Gomez-Paloma, *Angew. Chem. Int. Ed.* **2006**, *45*, 224–228.
[26] S. Chirayil, Q. Wu, C. Amezcua, K. J. Luebke, *PLoS One* **2014**, *9*, e108231.
[27] D. A. Case, H. M. Aktulga, K. Belfon, I. Y. Ben-Shalom, J. T. Berryman, S. R. Brozell, D. S. Cerutti, T. E. Cheatham, III, G. A. Cisneros, V. W. D. Cruzeiro, T. A. Darden, R. E. Duke, G. Giambasu, M. K. Gilson, H. Gohlke, A. W. Goetz, R. Harris, S. Izadi, S. A. Izmailov, K. Kasavajhala, M. C. Kaymak, E. King, A. Kovalenko, T. Kurtzman, T. S. Lee, S. LeGrand, P. Li, C. Lin, J. Liu, T. Luchko, R. Luo, M. Machado, V. Man, M. Manathunga, K. M. Merz, Y. Miao, O. Mikhailovskii, G. Monard, H. Nguyen, K. A. O'Hearn, A. Onufriev, F. Pan, S. Pantano, R. Qi, A. Rahnamoun, D. R. Roe, A. Roitberg, C. Sagui, S. Schott-Verdugo, A. Shajan, J. Shen, C. L. Simmerling, N. R. Skrynnikov, J. Smith, J. Swails, R. C. Walker, J. Wang, J. Wang, H. Wei, R. M. Wolf, X. Wu, Y. Xiong, Y. Xue, D. M. York, S. Zhao, P. A. Kollman, *Amber 2022*, University of California, San Francisco (USA), **2020**.
[28] Chemical Computing Group ULC, *Molecular Operating Environment (MOE), v2019.01*, 1010 Sherbooke St. West, Suite #910, Montreal, QC, Canada, H3 A 2R7, **2021**.
[29] M. Zgarbová, M. Otyepka, J. Šponer, A. Mládek, P. Banáš, T. E. I. Cheatham, P. Jurečka, *J. Chem. Theory Comput.* **2011**, *7*, 2886–2902.
[30] T. Steinbrecher, J. Latzer, D. A. Case, *J. Chem. Theory Comput.* **2012**, *8*, 4405–4412.
[31] S. Izadi, R. Anandakrishnan, A. V. Onufriev, *J. Phys. Chem. Lett.* **2014**, *5*, 3863–3871.
[32] M. Ester, H.-P. Kriegel, X. Xu, *A Density-Based Algorithm for Discovering Clusters in Large Spatial Databases with Noise*, United States: N. p., **1996**.
[33] J. Shao, S. W. Tanner, N. Thompson, T. E. Cheatham, *J. Chem. Theory Comput.* **2007**, *3*, 2312–2334.
[34] J. N. Ayres, K. B. Ling, L. C. Morrill, *Org. Lett.* **2016**, *18*, 5528–5531.
[35] a) G. A. Molander, F. Cadoret, *Tetrahedron Lett.* **2011**, *52*, 2199–2202; b) H. Li, C. Gascó, A. Delalande, C. Charnay, L. Raehm, P. Midoux, C. Pichon, R. Pleixats, J.-O. Durand, *Molecules* **2020**, *25*, 974.
[36] D. Llerena, O. Buisine, C. Aubert, M. Malacria, *Tetrahedron* **1998**, *54*, 9373–9392.
[37] N. Fuller, J. Lowe, *Bicyclic Inhibitors of Histone Deacetylase*, WO2019032528 (A1), **2019**.

Manuscript received: March 15, 2023
Accepted manuscript online: April 20, 2023
Version of record online: May 31, 2023